electronics

MDPI

Article

Multi-Parameter Estimation for an S/S Compensated IPT Converter Based on the Phase Difference between Tx and Rx Currents

Ligang Xu, Guangjie Ke, Qianhong Chen *, Bin Zhang, Xiaoyong Ren and Zhiliang Zhang

College of Automation Engineering, Nanjing University of Aeronautics and Astronautics, Nanjing 211106, China; xlg324@163.com (L.X.); kegaungjie@nuaa.edu.cn (G.K.); 1987bin@nuaa.edu.cn (B.Z.); renxy@nuaa.edu.cn (X.R.); zlzhang@nuaa.edu.cn (Z.Z.)

* Correspondence: chenqh@nuaa.edu.cn

Abstract: This paper proposes a multi-parameter estimation method based on the phase difference between primary and secondary currents, for a series/series (S/S) compensated contactless converter. To achieve secondary current sensing in the transmitter side, a primary sensing coil is added into the coupler. By introducing the phase difference between primary and secondary currents, a straightforward, multi-parameter estimation model is derived, significantly reducing the multi-parameter solving difficulty. Based on the derived model, a method combining pre-parameter identification based on frequency sweeping, with fast online parameter identification is proposed, offering a general, accurate, and rapid parameter estimation solution. Detailed implementation of the parameter identification method and the asymmetrical configuration of the coupler are also presented. The proposed method is verified with a 1 kW S/S compensated converter. Experimental results show that the estimated values agree well with the theoretical ones. Based on the estimated results, the transmitter-side, closed-loop control can also be achieved.

Keywords: parameter estimation; transmitter-side control strategy; wireless power transfer; constant current and constant voltage output

Citation: Xu, L.; Ke, G.; Chen, Q.; Zhang, B.; Ren, X.; Zhang, Z. Multi-Parameter Estimation for an S/S Compensated IPT Converter Based on the Phase Difference between Tx and Rx Currents. *Electronics* **2022**, *11*, 1023. https://doi.org/10.3390/electronics11071023

Academic Editor: Anna Richelli

Received: 4 March 2022
Accepted: 21 March 2022
Published: 24 March 2022

1. Introduction

Due to its advantages of isolation, safety, convenience, and reliability, inductive power transfer (IPT) technology has been used in many applications, such as underwater devices, implantable devices, electric vehicles, and high-voltage isolated power supplies [1–4]. Different from conventional power converters, IPT converters have the problem of a wide range of parameter variations, which include not only the load change, but also the variations of the self-inductances and mutual inductance of the coupler, due to the inevitable change of the clearance and misalignment. Hence, it greatly increases the difficulty of the control for IPT converters [5,6].

To achieve tight output control against the parameter variations, a post regulator in the receiver side is often adopted in an IPT system, by introducing a cascaded DC/DC converter, a secondary dynamic-tuned resonant tank [7,8], or an active rectifier [9,10]. It dramatically complexes the system's structure. By comparison, a transmitter-side (Tx-side) controller has the advantages of simplicity, lightness, and cost-effectiveness, especially for low- and medium-power applications. Numerous Tx-side control strategies, for instance, variable frequency control, phase shift control, pulse density modulation [11] and DC/DC conversion, have been applied in IPT systems. To realize closed-loop control, the output voltage/current should be sensed and fed back to the Tx side accurately and timely. Hence, real-time wireless communication approaches, such as Wi-Fi, Bluetooth, and ZigBee, are used to send the information of output voltage/current to the Tx side [12–14]. However, they suffer from the issues of disconnection, high latency, desynchrony, and interference.

As a more reliable alternative, Tx-side parameter estimation methods have been proposed and investigated in recent years [15–24].

As shown in Table 1, the parameter identification methods for the IPT system can be classified into two categories. One is based on a steady-state circuit model, and the other is based on the transient model, i.e., to construct the identification equations according to the dynamic response. Based on the amplitude decay rate of the voltage or current in the transient process, [15,16] presented the load resistance estimations for series/series (S/S) compensated converters operating at the self-oscillating frequency. However, the identification of the variable coil inductance and the mutual inductance, which affect the output voltage/current gain and the estimation of V_o and I_o, was not mentioned in them.

Table 1. Main transmitter-side parameter estimation methods.

Parameter Identification Methods		Compensations	Identified Variables	Operating Frequency	Ref.
Transient model	Free oscillation damping model	S/S	R_L (>50 Ω)	Self-oscillating frequency	[15]
			R_L (<25 Ω)	Self-oscillating frequency	[16]
Steady-state model	Phasor analysis	LCL/P	Vo and M	Fixed at resonant frequency	[17]
		S/S	R_L and M	Tracking primary resonant frequency	[18]
			M	Frequency with zero input phase angle	[19]
			M, r_2	Fixed at resonant frequency	[20]
			R_L and M	Different from ω_2	[21]
	Energy conservation	S/S	Reflected impedance	Fixed at resonant frequency	[22]
	Curve fitting	S/S	M and equivalent load	Fixed at resonant frequency	[23]
			Q_1, Q_2, ω_1, ω_2, L_1, L_2, and k	/	[24]

Note: Vo is the output voltage and R_L is the load resistance. M and k represent the mutual inductance and the coupling coefficient between the transmitting and receiving coils. r_2 is the parasitic resistance of the secondary coil. L_1, L_2, Q_1, and Q_2 represent the self-inductances and quality factors of the two coils of the coupler, respectively. ω_1 and ω_2 represent the resonant frequencies of the transmitter and the receiver, respectively.

Steady-state models are widely used in IPT systems for parameter estimation. Among them, an identification algorithm derived with phasor analysis is the normally used one [17–21]. In [17], identification of the mutual inductance and the output voltage for a secondary parallel compensated converter was conducted by analyzing the real and imaginary part of the reflected impedance under resonance. According to the phasor analysis under the conditions of switched compensation capacitors [18], shorted secondary circuit [19], special operating frequency [17–20] or startup process with variable duty cycle [19,20], and mutual inductance or load can be estimated. Reference [22] presents another method. It established the identification equations based on energy conservation and the characteristics of the zero-crossing point of the current in the transmitting (Tx) coil. However, most methods have special a requirement for the operating frequency, as shown in Table 1. Moreover, aforementioned methods are performed with the assumption of a constant self-inductance for the receiving (Rx) coil. Considering that the self-inductances and the resistances of the Tx and Rx coils vary with different displacements, it is necessary to perform a multi-parameter estimation including them, for achieving an accurate transmitter-side output control. Thus, [24] proposed a multi-parameter estimation method, including coil inductances and quality factors based on the curve fitting method, by using an optimization algorithm to iteratively solve the estimated parameters. However, due to a large number of iterations in the data processing, the estimation time is too long to be applied in real-time control.

The purpose of this article is to propose a multi-parameter estimation method for S/S compensated converters, which features generality, i.e., without operating frequency limitation, and with high accuracy and identification efficiency, suitable for Tx-side real-time control. This paper is organized as follows. In Section 2, the parameter estimation model of the S/S compensated converter, based on the phase difference between Tx and Rx currents, is proposed, as well as the estimation method combining pre-parameter identification based on frequency-sweeping, with fast online parameter identification. Detailed implementation of the proposed parameter estimation method is described in Section 3. Then, Section 4 proposes an asymmetric structure of the coupler, suitable for parameter estimation. Using a 1 kW S/S compensated converter, the proposed identification method is experimentally verified in Section 5. In Section 6, a conclusion of this article is conducted.

2. Parameter Estimation Method Based on the Phase Difference between Tx and Rx Current

2.1. Multi-Parameter Estimation Model

Figure 1 shows the schematic diagram of the S/S compensated converter, in which Q_1~Q_4 are power MOSFETs constituting an inverter, D_1~D_4 are secondary rectifier diodes, and R_L is the load resistor. Powered by a DC input voltage, V_{in}, the inverter produces an AC voltage, v_1 (current i_1), driving a resonant tank consisting of two compensation capacitors of C_1 and C_2, two equivalent series resistances of r_1, r_2, and a coupler. The coupler has a primary inductance, L_1, secondary inductance, L_2, and mutual inductance, M_{12}. The resonant tank delivers an AC current, i_2, which, after being rectified and filtered, gives the DC voltage Vo and current Io. It should be noted that r_1 and r_2 are the total equivalent series resistances in the primary and secondary circuits, which include the parasitic resistances of L_1, C_1, L_2, C_2, and the MOSFETs.

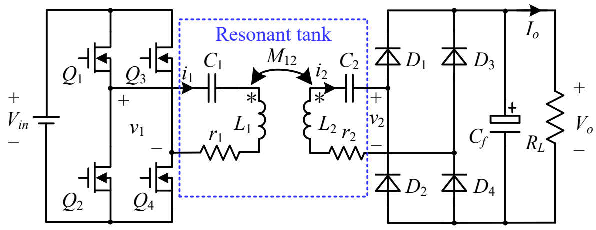

Figure 1. S/S compensated converter.

Using the fundamental harmonic approximation, the equivalent circuit of the S/S compensated converter can be obtained, as shown in Figure 2. In the figure, all voltage and current variables are represented by fundamental phasors, and the rectifier is represented by an equivalent resistance R_E.

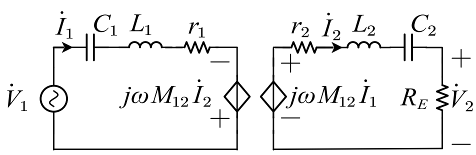

Figure 2. Equivalent circuit of the S/S compensated converter.

With the help of Fourier analysis, we have

$$V_1 = \frac{2\sqrt{2}}{\pi} V_{in}, V_2 = \frac{2\sqrt{2}}{\pi}(V_o + 2V_F),\ I_2 = \frac{\pi}{2\sqrt{2}} I_o \tag{1}$$

where V_1, V_2, and I_2 stand for the root-mean-square values of the fundamental components of v_1, v_2, and i_2, and V_F is the forward voltage drop of the rectifier diode.

Then, R_E can be obtained as

$$R_E = \frac{V_2}{I_2} = \frac{8}{\pi^2}\frac{V_o + 2V_F}{I_o} = \frac{8}{\pi^2}\left(R_L + \frac{2V_F}{I_o}\right) \approx \frac{8}{\pi^2}R_L \tag{2}$$

Since $2V_F/(IoR_L)$ is normally less than 5% for ensuring a high efficiency, the effect of V_F on R_E can be neglected.

By using Kirchhoff's voltage law, we have

$$\begin{bmatrix} V_1\angle 0^\circ \\ 0 \end{bmatrix} = \begin{bmatrix} jX_1 + r_1 & j\omega M_{12} \\ j\omega M_{12} & jX_2 + r_2 + R_E \end{bmatrix}\begin{bmatrix} I_1\angle\varphi \\ I_2\angle\theta \end{bmatrix} \tag{3}$$

where

$$X_1 = \omega L_1 - \frac{1}{\omega C_1} = \frac{1}{\omega C_1}\left(\frac{\omega^2}{\omega_p^2} - 1\right), X_2 = \omega L_2 - \frac{1}{\omega C_2} = \frac{1}{\omega C_2}\left(\frac{\omega^2}{\omega_s^2} - 1\right) \tag{4}$$

ω represents the operating angular frequency; ω_p and ω_s are the resonant angular frequencies of Tx and Rx sides, equaling to $\frac{1}{\sqrt{L_1C_1}}$, and $\frac{1}{\sqrt{L_2C_2}}$, respectively; φ and θ are the phase angles for $\dot{I}_1$ and $\dot{I}_2$, referring to $\dot{V}_1$.

Expanding the real parts and imaginary parts of (3), yields

$$\begin{cases} X_1 I_1 \cos\varphi + r_1 I_1 \sin\varphi - \omega M_{12} I_2 \cos\theta = 0 \\ -X_1 I_1 \sin\varphi + r_1 I_1 \cos\varphi + \omega M_{12} I_2 \sin\theta = V_1 \\ \omega M_{12} I_1 \cos\varphi - X_2 I_2 \cos\theta - (r_2 + R_E) I_2 \sin\theta = 0 \\ -\omega M_{12} I_1 \sin\varphi + X_2 I_2 \sin\theta - (r_2 + R_E) I_2 \cos\theta = 0 \end{cases} \tag{5}$$

Equations of (2), (4), and (5) provide the fundamental parameter estimation model for the S/S converter. Where, ω is a known parameter determined by the controller of the IPT system; φ, V_1, and I_1 can be directly measured on the Tx side; C_1, C_2, and V_F can be known prior to charging; L_1, L_2, M_{12}, r_1, V_o, I_o, and R_L are the parameters that need to be estimated. To facilitate the parameter identification, a primary sensing coil is introduced into the coupler for the detection of θ. As shown in Figure 3, the sensing coil has a self-inductance, L_3, mutual inductance, M_{23}, coupling with Rx coil, and mutual inductance, M_{13}, coupling with Tx coil. Adopting a decoupled configuration between Tx and sensing coils, M_{13} can approximate to zero. Hence, the phase θ of $\dot{I}_2$ can be obtained in Tx side by the open-circuit voltage, $\dot{V}_3$, across the sensing coil, which satisfies

$$\dot{V}_3 = j\omega M_{23}\dot{I}_2 - j\omega M_{13}\dot{I}_1 \approx j\omega M_{23}\dot{I}_2\Big|_{M_{13}\approx 0} \tag{6}$$

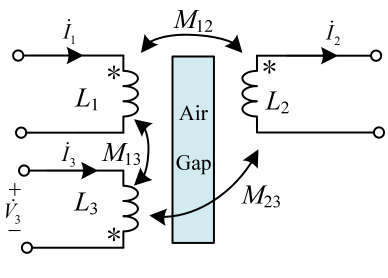

Figure 3. Contactless transformer with a primary sensing coil.

Further, the phase difference, γ, between i_1 and i_2 can be obtained. Substituting $\gamma = \varphi - \theta$ into (5), yields

$$r_1 I_1 + \omega M_{12} I_2 \sin\gamma = V_1 \cos\varphi \tag{7}$$

$$X_1 I_1 - \omega M_{12} I_2 \cos\gamma = -V_1 \sin\varphi \tag{8}$$

$$X_1 I_1 \sin\gamma + r_1 I_1 \cos\gamma = V_1 \cos\theta \tag{9}$$

$$X_2 \sin\gamma - (r_2 + R_E)\cos\gamma = 0 \tag{10}$$

$$\omega M_{12} I_1 \sin\gamma - (r_2 + R_E) I_2 = 0 \tag{11}$$

$$\omega M_{12} I_1 \cos\gamma - X_2 I_2 = 0 \tag{12}$$

The deriving procedure is provided in Appendix A.

Combining (7) and (12) with (4), and eliminating I_2 and X_2, gives

$$\frac{\omega^3 \sin 2\gamma C_2}{2[(\omega^2/\omega_s^2) - 1]} M_{12}^2 + r_1 = \frac{V_1 \cos\varphi}{I_1} \tag{13}$$

In (13), M_{12} and r_1 are independent of other parameters to be estimated. So, (13) gives a simple identification equation for M_{12} and r_1. Substituting the identified value of M_{12} and r_1 into (7) and (11), the values of I_2 and (r_2 + R_E) can be obtained. Then, according to (2), V_o, I_o, and R_E can be identified easily. It can be seen that, by introducing the phase difference between i_1 and i_2, a straightforward, multi-parameter estimation method can be derived.

However, the determination of ω_s and the efficient solving of (13) are still two important issues. In order to avoid any limitations on the operating frequency, we propose a frequency-sweeping method so as to obtain ω_s and other required information for the solving of (13). By selecting some special points with simplified equations for parameter identification, the solving efficiency can be improved. Thus, the process of the multi-parameter identification comprises two steps. Before charging, a frequency sweeping is performed for the IPT system under weak excitation. As a result, M_{12}, L_1, L_2, and r_1 can be determined prior to charging. During charging, V_o, I_o, and R_E can be identified rapidly online, based on the obtained parameters during frequency sweeping. At the same time, a Tx-side close-loop control for the IPT system can be realized. The proposed two-step parameter estimation method is suitable for static wireless charging applications, since M_{12}, L_1, L_2, and r_1 do not change during charging.

Next, detailed identifications of the parameters will be described.

2.2. Parameter Estimation during Frequency Sweeping

Firstly, we will discuss how to determine ω_s through frequency sweeping.

It can be seen from (6) that $\dot{V}_3$ is 90° ahead of $\dot{I}_2$ when M_{13} approximates to zero. By frequency sweeping, it is easy to find a frequency at which $\dot{V}_3$ is in the phase of $\dot{I}_1$, meaning γ = 90°. Substituting γ = 90° into (9) and (10), and combining (4), we have

$$\gamma = 90^\circ : X_1 = \frac{1}{\omega C_1}\left(\frac{\omega^2}{\omega_p^2} - 1\right) = \frac{V_1 \cos\theta}{I_1},\ X_2 = \frac{1}{\omega C_2}\left(\frac{\omega^2}{\omega_s^2} - 1\right) = 0 \tag{14}$$

It indicates that the angular frequency, ω, corresponding to γ = 90° is just the secondary resonance frequency, *ωs.*

Substituting $\omega s = \omega$ into (14) yields

$$\gamma = 90^\circ : \begin{cases} \omega_s = \omega \\ \omega_p = \omega\sqrt{\frac{I_1}{V_1 \omega C_1 \cos\theta + I_1}} \end{cases} \tag{15}$$

That means, by detecting the values of ω, V_{in}, I_1, and θ, corresponding to γ = 90°, both ω_s and ω_p can be obtained.

Then, substituting ω_s and ω_p into $\omega_p = \frac{1}{\sqrt{L_1 C_1}}$ and $\omega_s = \frac{1}{\sqrt{L_2 C_2}}$, L_1 and L_2 can be calculated.

At last, we will discuss how to solve (13) to identify M_{12} and r_1.

As can be seen from (13), there are two unknown parameters (M_{12} and r_1), but only one equation. During frequency sweeping, multiple sets of variables (ω, γ, φ, V_1, and I_1) can be measured, ensuring that (13) can be easily solved.

Defining

$$x_1(\omega) \;=\frac{\omega^2 \sin 2\gamma}{2X_2}=\frac{\omega^3 C_2 \sin 2\gamma}{2(\omega^2/\omega_s^2-1)}, x_2(\omega) \;=\frac{V_1 \cos\varphi}{I_1} \tag{16}$$

Equation (13) can be rewritten as

$$x_1(\omega)M_{12}^2+r_1-x_2(\omega)=0 \tag{17}$$

Equation (17) can be iteratively solved using an optimization algorithm, or directly solved adopting two special cases. We choose the latter for efficient solving. By using two sets of measured variables (ω, γ, φ, V_1, and I_1) at frequencies ω_1 and ω_2, the values of M_{12} and r_1 can be solved as

$$\begin{aligned} M_{12} &= \sqrt{\tfrac{x_2(\omega_1)-x_2(\omega_2)}{x_1(\omega_1)-x_1(\omega_1)}} \\ r_1 &= \tfrac{x_1(\omega_2)x_2(\omega_1)-x_2(\omega_2)x_1(\omega_1)}{x_1(\omega_2)-x_1(\omega_1)} \end{aligned} \tag{18}$$

To facilitate the signal sensing and equation solving, we chose ω_1 as the corresponding frequency when v_1 is in-phase with i_2, i.e., θ = 0, and ω_2 as (ω_1 + ω_s) / 2. Other frequency selections are also feasible. However, the selection of ω_1 and ω_2 should be avoided around the frequency corresponding to γ = 90° or φ = 90°, near which the slopes of the functions sin2γ and cosφ are relatively large, having a large phase detection error.

2.3. Online Parameter Estimation

Substituting the identified value of M_{12} and r_1 into (7) and (11), we have.

$$I_2=(V_1\cos\varphi-r_1I_1)/(\omega M_{12}\sin\gamma) \tag{19}$$

$$V_2=R_EI_2=\frac{\omega M_{12}I_1\sin\gamma}{1+r_2/R_E}\approx\omega M_{12}I_1\sin\gamma \tag{20}$$

Normally, r_2/R_E is less than 3% for achieving a high efficiency. Thus, 1 + $r_2/R_E \approx 1$ in (20).

Substituting (1) into (19) and (20), V_o and I_o can be derived

$$I_o=\frac{0.81V_{in}\cos\varphi-0.9r_1I_1}{\omega M_{12}\sin\gamma} \tag{21}$$

$$V_o\approx 1.11\omega M_{12}I_1\sin\gamma-2V_F \tag{22}$$

Since M_{12}, r_1, and V_F are known parameters, and V_{in}, I_1, φ, γ, and ω can be measured online, the real-time identification of V_o and I_o can be realized.

Combining (11) and (12) with (4), gives

$$R_E+r_2=X_2\tan\gamma=\frac{1}{\omega C_2}\left(\frac{\omega^2}{\omega_s^2}-1\right)\tan\gamma \tag{23}$$

Combining (23) with (2), R_L can be obtained as

$$R_L\approx\frac{\pi^2}{8}R_E=\frac{\pi^2}{8}\frac{1}{\omega C_2}\left(\frac{\omega^2}{\omega_s^2}-1\right)\tan\gamma \tag{24}$$

Besides, according to (6), we can calculate the value of M_{12} online, denoted as $\hat{M}_{12}$, satisfying

$$\hat{M}_{12} = \sqrt{\frac{2}{\sin 2\gamma}\frac{1}{\omega^3 C_2}\left(\frac{\omega^2}{\omega_s^2} - 1\right)\left(\frac{V_1 \cos\varphi}{I_1} - r_1\right)} \quad (25)$$

According to the value of $\hat{M}_{12}$ and the difference between $\hat{M}_{12}$ and M_{12}, we can judge if the Rx pad is still in the charging region, thereby improving the reliability of the IPT system.

3. Implementation of the Proposed Estimation Method

3.1. Diagram of the IPT System

According to the proposed estimation method in Section 2, the diagram of the IPT system with the Tx-side circuit can be illustrated, as shown in Figure 4, where S_1 is used for operating state switching. When S_1 is connected with R_O, the IPT system will operate in a frequency-sweeping state under weak excitation, for pre-parameter-identification. When S_1 is connected with R_L, the IPT system will operate in a normal charging state, and the online parameter identification is achieved. As shown in Figure 4, v_3 and i_3 are converted to square wave signals by the zero detector, to facilitate the detection of φ, θ, and γ. After the parameter estimation, the values of L_1, L_2, M_{12}, r_1, Vo, Io, and R_L can be obtained. Based on them, a Tx-side, closed-loop control can be conducted.

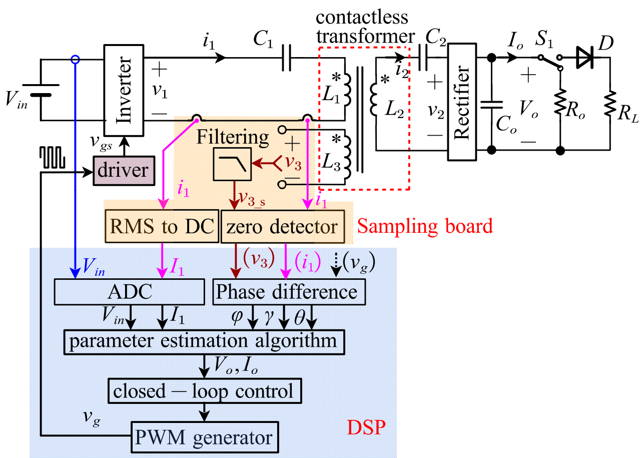

Figure 4. Diagram of IPT system with Tx- side circuit.

3.2. Flowchart of the Parameter Estimation

Figures 5 and 6 illustrate the flowcharts of the proposed parameter estimation algorithm, where the values of γ, φ, θ, V_{in}, and I_1 are measured by the sensors, ω can be obtained by the controller, and V_1 can be calculated by (2).

First, the offline parameter estimation is conducted. As shown in Figure 5, ω_s and ω_1 are obtained by sweeping the operating frequency f from f_{min} to f_{max}. The controller measures γ and θ at each frequency, and compares them with 90° and 0°, respectively. When γ = 90°, the corresponding operating frequency is recorded as ω_s; when θ = 90°, the corresponding frequency is recorded as ω_1. ε is the allowable error. Then, based on ω_s and ω_1, the operating angular frequency is adjusted, and the three groups of variables (ω, γ, φ, θ, V_{in}, and I_1) are measured at different frequencies to calculate ω_p, M_{12}, and r_1.

After finishing the offline parameter estimation, the online real-time identification of load variables (V_o, I_o, and R_L) can be realized, as shown in Figure 6. During the operation, $\hat{M}_{12}$ is estimated and compared with M_{12} to judge if the Rx pad is in the allowable charging region.

It is worth noting that the proposed estimation method has no operating frequency limitations. Besides, the proposed identification model has considered the effect of r_1 and V_F, offering high accuracy.

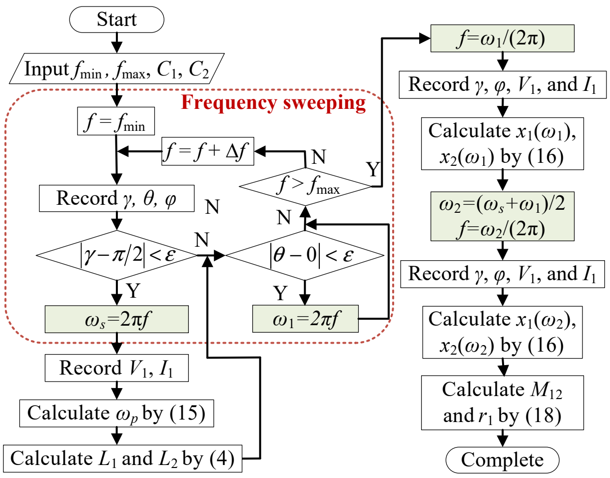

Figure 5. Flowchart of the off-line parameter estimation.

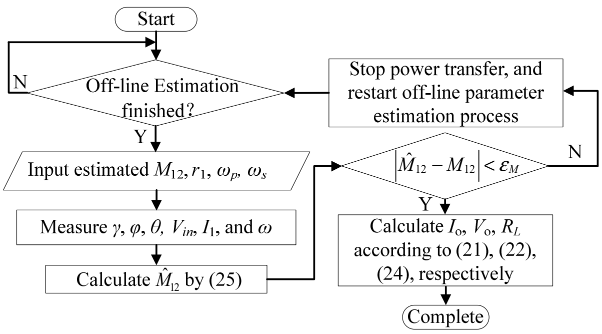

Figure 6. Flowchart of the online parameter estimation.

4. Configuration of the Magnetic Coupler

For the IPT system as shown in Figure 4, the contactless transformer is a crucial part, not only for power transfer but also for phase detection of the secondary current. In this section, we will discuss how to determine its configuration.

4.1. Proposed Asymmetrical Configuration

As indicated in (6), to realize an accurate phase detection, the contactless transformer is required to have a nearly zero M_{13} and nonzero M_{23}. That means the sensing coil should always be decoupled with Tx coil and coupled with Rx coil. In previous studies, [25] has presented several decoupled configurations for achieving a nearly zero M_{13}. However, they also make M_{23} zero when Rx coil is exactly aligned with Tx coil. To satisfy the requirements, an asymmetric structure of the coupler is proposed. As shown in Figure 7, the coupler adopts different sizes for Tx and Rx pads, and the sensing coil is divided into two asymmetric segments, L_{C1} and L_{C2}.

To obtain the zero coupling ($M_{13} = 0$), two sub coils of the sensing coil, L_{C1} and L_{C2}, are concentrically placed on the Tx pad, and reversely connected in a series. Thus, the equivalent mutual inductance, M_{13}, can be expressed as

$$M_{13} = (N_{C1}\phi_{C1} - N_{C2}\phi_{C2})/i_1 \tag{26}$$

where N_{C1} and N_{C2} are the number of turns of L_{C1} and L_{C2}, and ϕ_{C1} and ϕ_{C2} represent the magnetic flux coupled by L_{C1} and L_{C2}, respectively. Both ϕ_{C1} and ϕ_{C2} are produced by the Tx coil, and they are the same sign. Then, by adjusting L_{C1} and L_{C2}, M_{13} can approach zero.

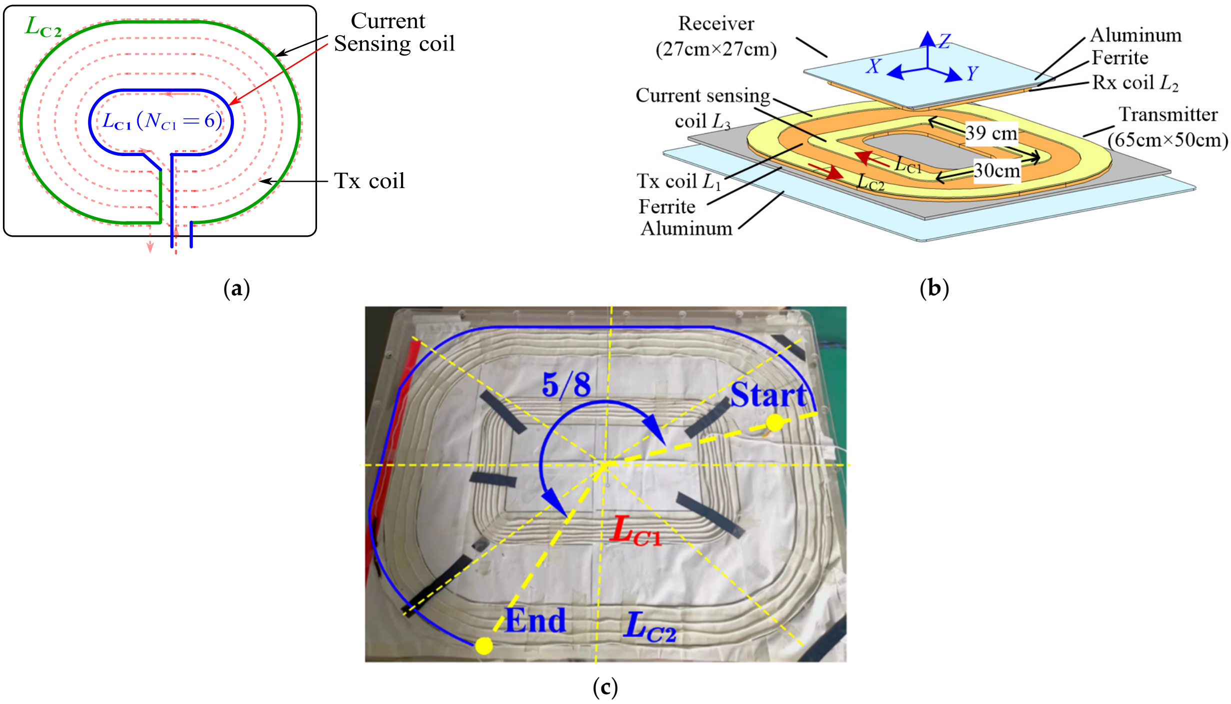

Figure 7. Asymmetric structure and dimensions of the coupler. (**a**) Two-dimensional graph of Tx pad, (**b**) three-dimensional graph of the coupler, and (**c**) practical configuration of the sensing coil.

The asymmetric structure for L_{C1} and L_{C2}, combining with the different size for Tx and Rx pads, ensures the nonzero M_{23} under both aligned and misaligned conditions.

4.2. Simulation Results

We choose the magnetic coupler recommended by SAE J2954-2017 as a design example. Detailed dimensions are as shown in Figure 7, and the clearance, ΔZ, ranges from 10–16 cm.

As shown in Figure 7a, L_{c1} is placed around the center of the Tx pad, with six turns for N_{C1}; L_{c2} is placed around the outer border of the Tx pad with N_{C2} turns. By measuring the mutual inductance with an LCR meter, we can easily find a proper value for N_{C2} to achieve a zero M_{12}. The practical configuration of the sensing coil is shown in Figure 7c. As seen, N_{C2} is about 4.7 since the outermost turn of L_{c2} is not fully wound.

We also use the software COMSOL to assist the design of the sensing coil. Figure 8 shows the curves of M_{13} and M_{23} versus N_{C2}. It can be seen that zero coupling (M_{13} = 0) occurs at the point of N_{C2} = 4.7, which also guarantees a nonzero M_{23}. When Tx and Rx pads are aligned, due to the asymmetrical configurations of the coupler and the sensing coil, the couplings between L_{c1}/ L_{c2} and Rx coil will not be completely offset, yielding a nonzero M_{23}. Besides, the simulated value of N_{C2} (4.7) for M_{13} = 0 matches the measured one very well.

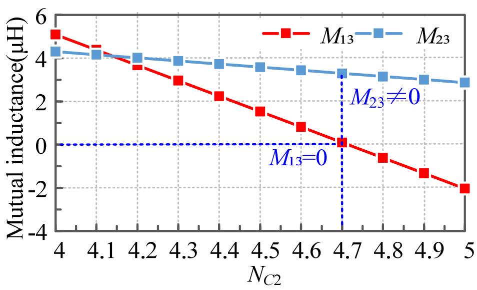

Figure 8. Simulated M_{13} and M_{23} versus N_{C2} (ΔX = ΔY = 0 and ΔZ = 13 cm).

Using N_{C1} = 6 and N_{C2} = 4.7, M_{13} and M_{23} are further simulated in the case of misalignments, as shown in Figure 9. It can be seen that M_{13} is close to zero and M_{23} is larger than zero within a wide range of misalignments, meeting the coupling requirements. Therefore, the proposed asymmetric configuration is suitable for phase detection.

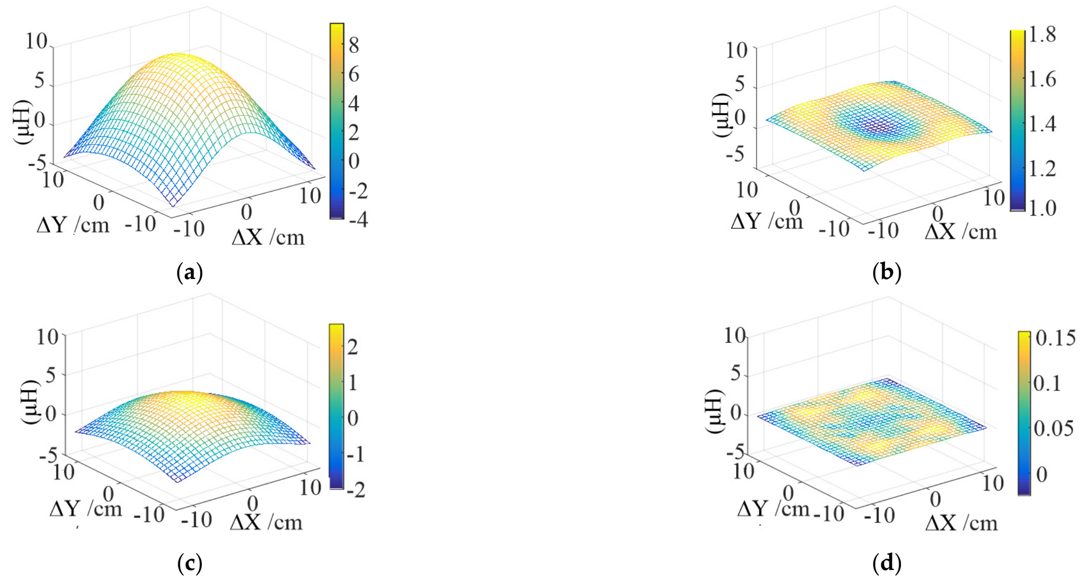

Figure 9. Simulated M_{13} and M_{23} under different misalignments at ΔZ = 10 cm: (**a**) M_{23} and (**b**) M_{13}. At ΔZ = 16 cm: (**c**) M_{23} and (**d**) M_{13}.

Since the sensing coil is mounted on the Tx pad, M_{13} is a constant, while M_{23} is a parameter sensitive to the relative position between Tx coil and Rx coil. As shown in Figure 9, M_{23} gradually decreases with increasing ΔX and ΔY. When M_{23} is reduced to zero, the sensing coil will lose the function for the phase detection, which should be avoided. Figure 10 illustrates the simulated zero coupling position of M_{23}. The radius of the effective coupling area is approximately 10 cm, satisfying the misalignment requirements (ΔX $\leq \pm$7.5 cm and ΔY $\leq \pm$10 cm) by the SAE J2954 standard.

Figure 10. Zero coupling position of M_{23} at a clearance of (**a**) ΔZ = 10 cm and (**b**) ΔZ = 16 cm.

5. Experimental Evaluation and Discussion

5.1. Experimental Prototype

To verify the above analysis, a 1 kW prototype was built and tested in the laboratory. Figure 11 shows the experimental setup for the built prototype. The system parameters are listed in Table 2. The variable frequency range is from 85 kHz to 100 kHz. Q_1~Q_4 are IXTV200N10T ($R_{DS(ON)}$ = 5.5 mΩ) and D_1~D_4 are DSEI120-06A (V_F = 0.7 V). The parameter estimation method and the closed-loop control are implemented in the DSP TMS320F28335 (150 MHz).

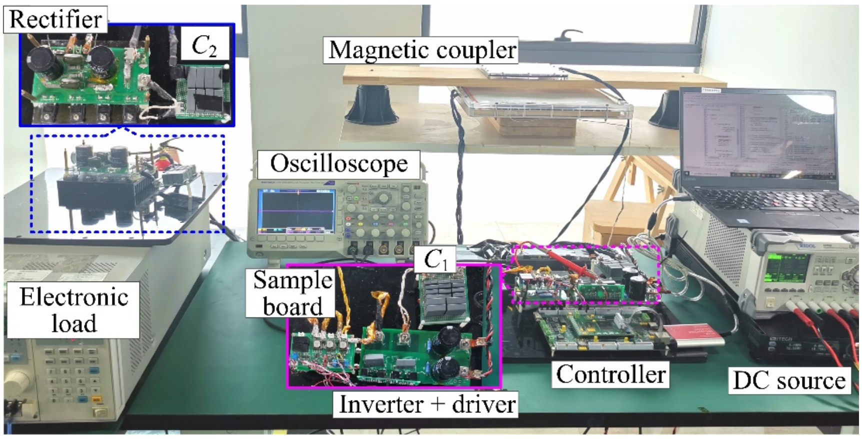

Figure 11. Photo of the prototype.

Table 2. IPT prototype parameters.

Components	Value	Components	Value
Input voltage	80 V	Output power	1 kW
Resonant frequency	85 kHz	Compensation	C_1 = 88.1 nF, r_{C1} = 41.2 mΩ
Clearance range	10–16 cm		C_2 = 94.5 nF, r_{C1} = 27.4 mΩ

The experimental verifications include three parts: (1) the verification of the phase-detection function; (2) the feasibility and accuracy of the proposed parameter estimation method; (3) the transmitter-side, closed-loop control with the estimated results.

5.2. Phase Detection of the Secondary Current

The practical inductances and coil resistances (r_{L1}, r_{L2}, and r_{L3}) of the proposed magnetic coupler are listed in Table 3. Figure 12 illustrates the variation of M_{12}, M_{23}, and M_{13} under misalignments and different clearance conditions. As expected, M_{13} is approximately zero within the required clearance range and a certain range of misalignments, while M_{23} is greater than zero, satisfying the coupling requirements discussed in Section 4.

Table 3. Measured parameters of the magnetic coupler.

ΔZ	L_1/μH	L_2/μH	L_3/μH	M_{12}/μH	M_{13}/μH	M_{23}/μH	r_{L1}/Ω	r_{L2}/Ω	r_{L3}/Ω
10 cm	42.56	38.66	47.26	10.62	0.165	8.36	0.065	0.06	0.28
13 cm	44.07	37.52	46.5	8.455	0.06	4.92			
16 cm	44.97	36.7	46.25	6.635	0.015	2.915			

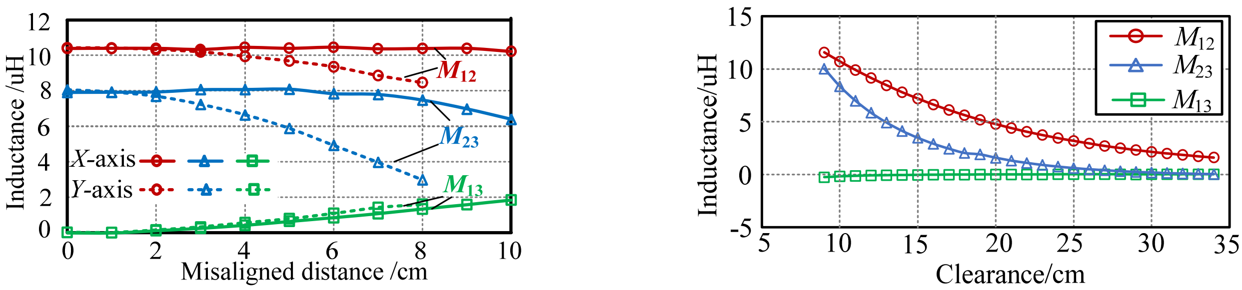

(**a**) (**b**)

Figure 12. Measured mutual inductances of M_{12}, M_{23}, and M_{13} under (**a**) misaligned conditions with ΔZ = 10 cm and (**b**) different clearance conditions with ΔX = ΔY = 0 cm.

To verify the phase-detection function of the sensing coil, the experimental waveforms of v_3, its filtered output, v_{3_s}, and i_2, are tested with different misalignments. As shown in

Figure 13, v_3 is distorted. To correct this distortion, a low-frequency filter with a 90° phase shift is adopted. In the waveforms, v_{3_s} and i_2 are always in-phase, and lag, v_3, is nearly 90°, agreeing with the theoretical analysis in (6). Therefore, the presented asymmetrical configuration of the coupler can accurately detect the phase information of i_2.

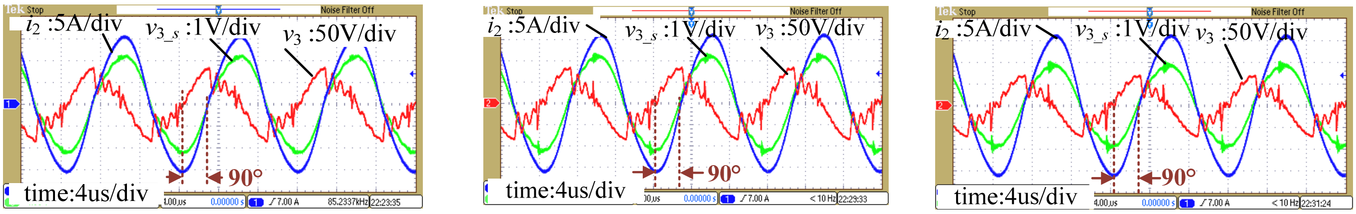

(**a**) (**b**) (c)

Figure 13. Experimental waveforms of v_3, v_{3_s}, and i_2 under the condition of (**a**) ΔX = ΔY = 0 cm; (**b**) ΔX = 0 cm and ΔY = 6 cm; (**c**) ΔX = 4 cm and ΔY = 0 cm. (ΔZ = 10cm).

5.3. Parameter Estimation Results

5.3.1. Offline Parameter Estimation

Offline parameter estimation is conducted under weak excitation with V_{in} = 30 V. Relay S_1 in Figure 4 is switched to the test resistor *Ro*, and *Ro* is fixed at 8 Ω during the estimation process. Following the procedure provided in Figure 5, M_{12}, L_1, L_2, and r_1 are obtained, as illustrated in Table 4 and Figure 14.

Table 4. Estimated results of M_{12}, L_1, L_2, and r_1 at different clearances.

ΔZ	Estimated Results				Estimation Error ε			
	L_1/μH	L_2/μH	M_{12}/μH	r_1/Ω	L_1/μH	L_2/μH	M_{12}/μH	r_1/Ω
10 cm	41.98	37.48	10.2	0.156	−1.3%	−3.05%	−3.95%	33.1%
13 cm	43.61	37.08	8.162	0.15	−1.04%	−1.17%	−3.47%	27.9%
16 cm	44.52	36.41	6.709	0.147	−1%	−0.08%	−1.12%	25.4%

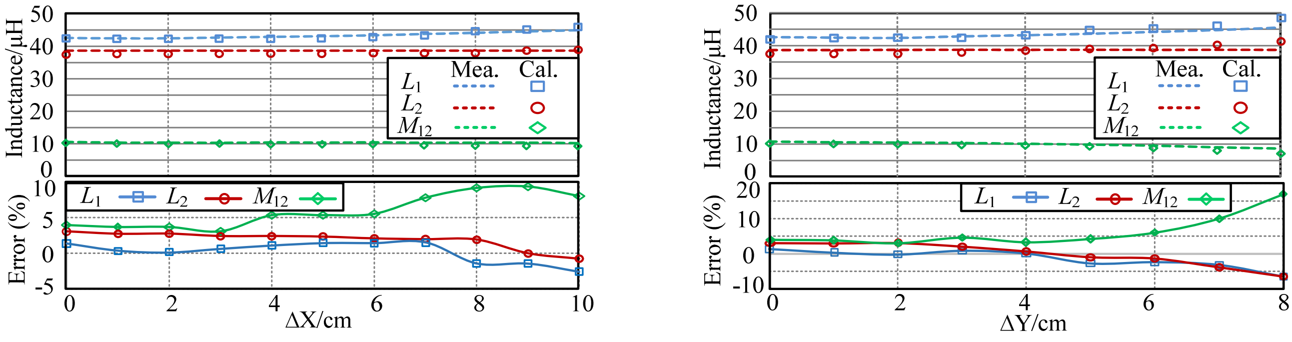

(**a**) (**b**)

Figure 14. Experimental results for the off-line estimation versus (**a**) ΔX; (**b**) ΔY.

Note that r_1 represents the total equivalent resistance in the transmitter circuit, and its measured value is calculated as the sum of r_{L1}, r_{C1}, and $R_{DS(ON)}$.

$$r_{1\_\text{mea}} \approx 2R_{DS(ON)} + r_{L1} + r_{C1} = 117.2 \text{ m}\Omega \tag{27}$$

To evaluate the accuracy of the estimation, the estimation error is defined as

$$\varepsilon = (\text{Mea.} - \text{Cal.})/\text{Mea.} \times 100\% \tag{28}$$

where Mea. and Cal. represent the measured and calculated values, respectively.

It can be seen from Table 4 that the ε for M_{12}, L_1, and L_2 are all less than 4%, indicating the high accuracy of the estimation method. However, the ε for r_1 is much larger. From (27), it can be noted that r_1 is only 117.2 mΩ. Thus, a small deviation will lead to a large error.

Figure 14 shows that the estimation accuracy is lower when the misaligned distance is relatively large. Hence, the misalignment should be set within a suitable range, to ensure estimation accuracy. Within the misaligned range of $\Delta X \leq 6$ cm and $\Delta Y \leq 6$ cm, the maximum identification error of M_{12} is 5.5%, the maximum identification error of L_1 is 3.9%, and the maximum identification error of L_2 is 3.6%.

5.3.2. Online Parameter Estimation

With the estimated M_{12}, L_1, L_2, and r_1, the online parameter estimation is carried out based on the estimation method in Figure 6. The relative position of the Tx coil and the Rx coil is fixed at (ΔX = 0 cm, ΔY = 0 cm, and ΔZ = 10 cm).

Figure 15 shows the measured and estimated values of V_o and I_o at various frequencies and load resistances. The frequency is changed from 85 kHz to 105 kHz, and R_o is varied from 6 Ω to 16 Ω. All the identification results are in good agreement with the measured ones, and the maximum ε is less than 8%. The feasibility and accuracy of the proposed identification method are well verified.

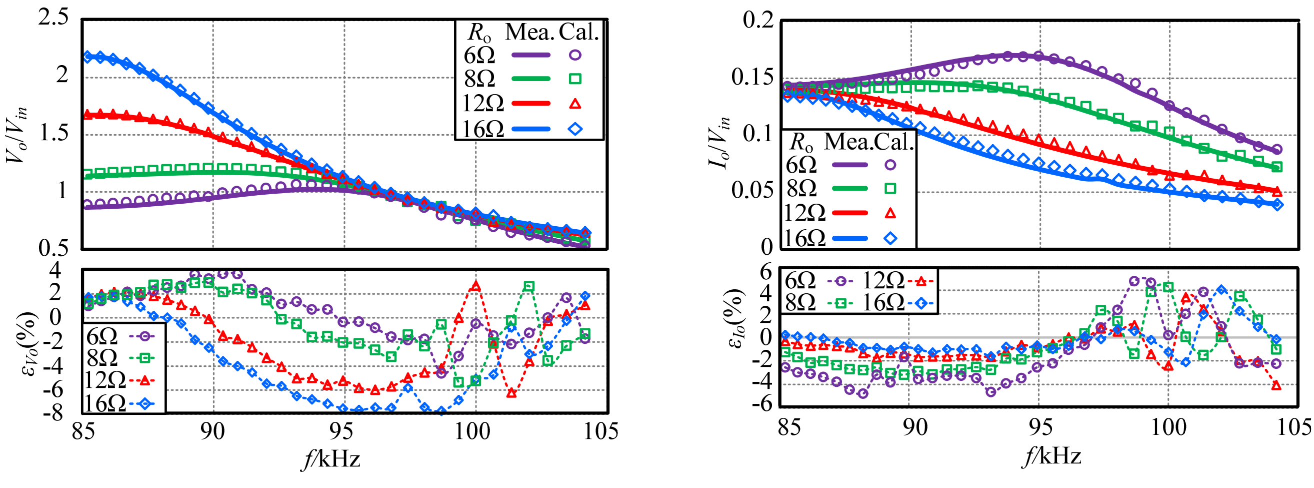

Figure 15. Identification results of the (**a**) output voltage and (**b**) output current at various frequencies and load resistances.

The online estimated values of M_{12} with different *Ro* are illustrated in Figure 16. The measured value (10.62 μH) and the offline estimated value (10.2 μH) are also marked in Figure 16 for comparison. As seen, the estimated $\hat{M}_{12}$ varies around M_{12}. Therefore, by comparing $\hat{M}_{12}$ with M_{12}, it can be detected whether there is abnormal movement during charging.

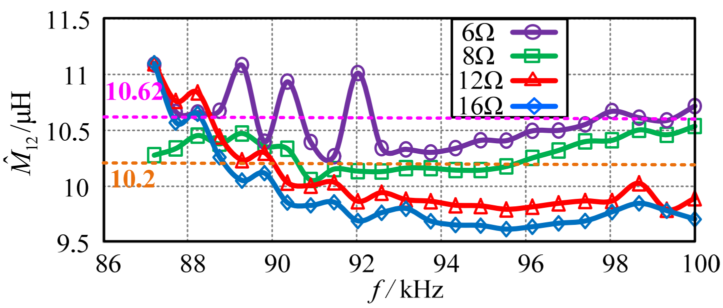

Figure 16. Online mutual inductance estimation results at different loads.

Figure 17 shows the identification results of R_L. The switching frequency is fixed at 85 kHz, and R_L is changed from 4 to 20 Ω. The estimated results coincide with the theoretical results, verifying the effectiveness of the proposed estimation method.

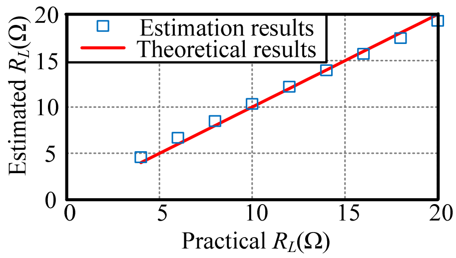

Figure 17. Identification results of the load resistance, R_L.

5.4. Closed-Loop Control Results

Based on the dynamically estimated values of V_o and I_o, constant current (CC) and constant voltage (CV) charging for S/S compensation are also achieved by employing only a transmitter controller. Here, the variable frequency control is employed. The operating frequency range is set as 85 kHz–100 kHz. The calculation time for I_o and V_o are listed in Table 5. As seen, the calculation time is smaller than the switching period. So, V_o and I_o can be identified rapidly during charging.

Table 5. Calculation time for I_o and V_o (TMS320F28335 150 MHz).

	Execution Cycle	Calculation Time
V_o	346	2.30667 μs
I_o	178	1.18667 μs

In the prototype, a bidirectional, programmable DC power supply of IT6006C-500-40 is used to imitate the characteristics of the battery. The parameters of the battery emulator are set as follows: an empty voltage of 56 V, a full voltage of 80 V, a negative/positive current limit value of 20 A, and an inner resistance of 10 mΩ. The target charging current for CC mode is set as 13 A. The battery-charging waveforms of V_o and I_o, and the measured efficiency, are shown in Figure 18. As seen in Figure 18a, both CC charging and CV charging are achieved. It demonstrates the effectiveness of the proposed parameter estimation method. The maximum efficiency is 88.6%.

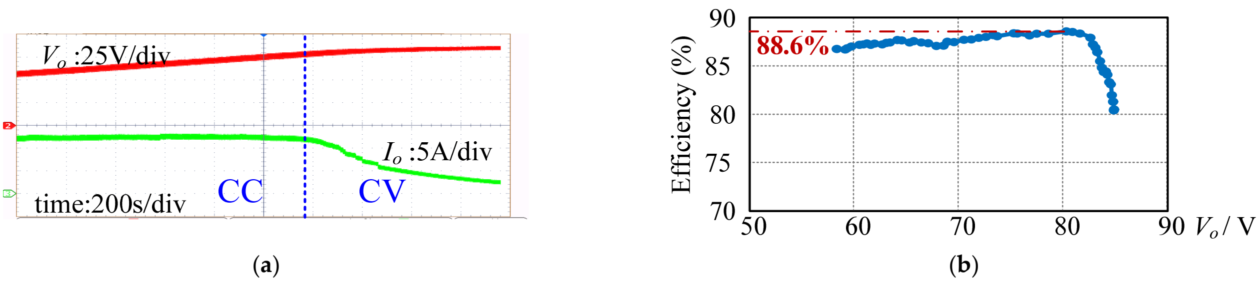

Figure 18. (**a**) Charging curves for closed-loop control and (**b**) corresponding efficiencies.

6. Conclusions

In this paper, a multi-parameter estimation method that utilizes the phase difference between primary and secondary currents is proposed for an S/S compensated contactless converter. This method has the advantages of generality, i.e., being without operating frequency limitation, and having high accuracy and identification efficiency, which is suitable for transmitter-side, real-time control. The detailed implementation of the parameter estimation method is studied. For realizing precise phase detection of the secondary current, a novel structure, which divides the sensing coil into two asymmetrical segments, is presented. A 1 kW wireless charger prototype is built for verification. The estimated results and the actual values are in close agreement, and the maximum identification error is less than 8%. Also, a closed-loop control is performed based on the estimated results.

Author Contributions: Conceptualization, L.X. and G.K.; methodology, L.X. and G.K.; software, B.Z.; validation, L.X., G.K. and Q.C.; formal analysis, L.X.; investigation, L.X. and G.K.; resources, Q.C., X.R. and Z.Z.; writing—original draft preparation, L.X. and G.K.; writing—review and editing, Q.C., X.R. and Z.Z.; supervision, Q.C.; project administration, L.X.; funding acquisition, L.X. and Q.C. All authors have read and agreed to the published version of the manuscript.

Funding: This work was supported by Jiangsu Provincial Industrial Prospective and the Key Core Technology Project of China, grant number BE2019113.

Conflicts of Interest: The authors declare no conflict of interest.

Appendix A

For clarity, the formulas in (5) are renumbered follows:

$$X_1 I_1 \cos\varphi + r_1 I_1 \sin\varphi - \omega M_{12} I_2 \cos\theta = 0 \tag{A1}$$

$$-X_1 I_1 \sin\varphi + r_1 I_1 \cos\varphi + \omega M_{12} I_2 \sin\theta = V_1 \tag{A2}$$

$$\omega M_{12} I_1 \cos\varphi - X_2 I_2 \cos\theta - (r_2 + R_E) I_2 \sin\theta = 0 \tag{A3}$$

$$-\omega M_{12} I_1 \sin\varphi + X_2 I_2 \sin\theta - (r_2 + R_E) I_2 \cos\theta = 0 \tag{A4}$$

Multiplying (A1) by sinφ and (A2) by cosφ, and then adding them up, gives

$$\begin{aligned} & r_1 I_1 \left(\sin^2\varphi + \cos^2\varphi\right) \ + \ \omega M_{12} I_2 (\sin\theta\cos\varphi - \cos\theta\sin\varphi) \ = V_1 \cos\varphi \\ \Rightarrow\ & r_1 I_1 + \omega M_{12} I_2 \sin(\theta - \varphi) \ = V_1 \cos\varphi \end{aligned} \tag{A5}$$

Substituting $\gamma = \varphi - \theta$ into (A5) yields (7).

Similarly, (8) can be derived by adding the product of (A1) and cosφ with the product of (A2) and ($-$sinφ), that is

$$\begin{aligned} & X_1 I_1 \left(\cos^2\varphi + \sin^2\varphi\right) - \ \omega M_{12} I_2 (\cos\theta\cos\varphi + \sin\theta\sin\varphi) \ = -V_1 \sin\varphi \\ \Rightarrow\ & X_1 I_1 - \omega M_{12} I_2 \cos(\theta - \varphi) \ = -V_1 \sin\varphi \\ \Rightarrow\ & X_1 I_1 - \omega M_{12} I_2 \cos\gamma = -V_1 \sin\varphi \ (8) \end{aligned} \tag{A6}$$

$(\mathrm{A1}) \cdot \sin\theta + (\mathrm{A2}) \cdot \cos\theta$ gives (9).

$$\begin{aligned} & X_1 I_1 (\cos\varphi\sin\theta - \sin\varphi\cos\theta) \ + \ r_1 I_1 (\sin\varphi\sin\theta + \cos\varphi\cos\theta) \ = V_1 \cos\theta \\ \Rightarrow\ & X_1 I_1 \sin(\theta - \varphi) + r_1 I_1 \cos(\theta - \varphi) \ = V_1 \cos\theta \\ \Rightarrow\ & X_1 I_1 \sin\gamma + r_1 I_1 \cos\gamma = V_1 \cos\theta \ (9) \end{aligned} \tag{A7}$$

The derivations (10)–(12) follow a likewise procedure and are omitted in this paper.

References

1. Covic, G.A.; Boys, J.T. Inductive Power Transfer. *Proc. IEEE* **2013**, *101*, 1276–1289. [CrossRef]
2. Cheng, Z.; Lei, Y.; Song, K.; Zhu, C. Design and Loss Analysis of Loosely Coupled Transformer for an Underwater High-Power Inductive Power Transfer System. *IEEE Trans. Magn.* **2015**, *51*, 1–10.
3. Ho, J.S.; Kim, S.; Poon, A.S.Y. Midfield Wireless Powering for Implantable Systems. *Proc. IEEE* **2013**, *101*, 1369–1378. [CrossRef]
4. Zhang, L.; Gu, S.J.S.; Huang, X.; Palmer, J.; Giewont, W.; Wang, F.; Tolbert, L.M. Design Considerations for High-Voltage Insulated Gate Drive Power Supply for 10-kV SiC MOSFET Applied in Medium-Voltage Converter. *IEEE Trans. Ind. Electron.* **2021**, *68*, 5712–5724. [CrossRef]
5. Ahmad, A.; Alam, M.S.; Chabaan, R. A Comprehensive Review of Wireless Charging Technologies for Electric Vehicles. *IEEE Trans. Transp. Electrification* **2018**, *4*, 38–63. [CrossRef]
6. Patil, D.; McDonough, M.K.; Miller, J.M.; Fahimi, B.; Wireless, P.T.B. Power Transfer for Vehicular Applications: Overview and Challenges. *IEEE Trans. Transp. Electrification* **2018**, *4*, 3–37. [CrossRef]

7. Hsu, J.U.W.; Hu, A.P.; Swain, A. A Wireless Power Pickup Based on Directional Tuning Control of Magnetic Amplifier. *IEEE Trans. Ind. Electron.* **2009**, *56*, 2771–2781. [CrossRef]
8. Beh, T.C.; Kato, M.; Imura, T.; Oh, S.; Hori, Y. Automated Impedance Matching System for Robust Wireless Power Transfer via Magnetic Resonance Coupling. *IEEE Trans. Ind. Electron.* **2013**, *60*, 3689–3698. [CrossRef]
9. Huang, Z.; Lam, C.-S.; Mak, P.-I.; Martins, R.P.d.; Wong, S.-C.; Tse, C.K. A Single-Stage Inductive-Power-Transfer Converter for Constant-Power and Maximum-Efficiency Battery Charging. *IEEE Trans. Power Electron.* **2020**, *35*, 8973–8984. [CrossRef]
10. Colak, K.; Asa, E.; Bojarski, M.; Czarkowski, D.; Onar, O.C. A Novel Phase-Shift Control of Semibridgeless Active Rectifier for Wireless Power Transfer. *IEEE Trans. Power Electron.* **2015**, *30*, 6288–6297. [CrossRef]
11. Li, H.; Wang, K.; Fang, J.; Tang, Y. Pulse Density Modulated ZVS Full-Bridge Converters for Wireless Power Transfer Systems. *IEEE Trans. Power Electron.* **2019**, *34*, 369–377. [CrossRef]
12. Li, H.; Fang, J.; Chen, S.; Wang, K.; Tang, Y. Pulse Density Modulation for Maximum Efficiency Point Tracking of Wireless Power Transfer Systems. *IEEE Trans. Power Electron.* **2018**, *33*, 5492–5501. [CrossRef]
13. Jiang, Y.; Wang, L.; Wang, Y.; Wu, M.; Zeng, Z.; Liu, Y.; Sun, J. Phase-Locked Loop Combined With Chained Trigger Mode Used for Impedance Matching in Wireless High Power Transfer. *IEEE Trans. Power Electron.* **2020**, *35*, 4272–4285. [CrossRef]
14. Yeo, T.D.; Kwon, D.; Khang, S.T.; Yu, J.W. Design of Maximum Efficiency Tracking Control Scheme for Closed-Loop Wireless Power Charging System Employing Series Resonant Tank. *IEEE Trans. Power Electron.* **2017**, *32*, 471–478. [CrossRef]
15. Wang, Z.H.; Li, Y.P.; Sun, Y.; Tang, C.S.; Lv, X. Load Detection Model of Voltage-Fed Inductive Power Transfer System. *IEEE Trans. Power Electron.* **2013**, *28*, 5233–5243. [CrossRef]
16. Hu, S.; Liang, Z.; Wang, Y.; Zhou, J.; He, X. Principle and Application of the Contactless Load Detection Based on the Amplitude Decay Rate in a Transient Process. *IEEE Trans. Power Electron.* **2017**, *32*, 8936–8944. [CrossRef]
17. Thrimawithana, D.J.; Madawala, U.K. A primary side controller for inductive power transfer systems. In Proceedings of the 2010 IEEE International Conference on Industrial Technology, Via del Mar, Chile, 14–17 March 2010.
18. Su, Y.G.; Zhang, H.Y.; Wang, Z.H.; Hu, A.P.; Chen, L.; Sun, Y. Steady-State Load Identification Method of Inductive Power Transfer System Based on Switching Capacitors. *IEEE Trans. Power Electron.* **2015**, *30*, 6349–6355. [CrossRef]
19. Liu, Y.; Madawala, U.K.; Mai, R.; He, Z. Primary-Side Parameter Estimation Method for Bi-Directional Inductive Power Transfer Systems. *IEEE Trans. Power Electron.* **2021**, *36*, 68–72. [CrossRef]
20. Liu, F.; Chen, K.; Zhao, Z.; Li, K.; Yuan, L. Transmitter-Side Control of Both the CC and CV Modes for the Wireless EV Charging System With the Weak Communication. *IEEE J. Emerg. Sel. Top. Power Electron.* **2018**, *6*, 955–965. [CrossRef]
21. Yin, J.; Lin, D.; Parisini, T.; Hui, S.Y. Front-End Monitoring of the Mutual Inductance and Load Resistance in a Series–Series Compensated Wireless Power Transfer System. *IEEE Trans. Power Electron.* **2016**, *31*, 7339–7352. [CrossRef]
22. Dai, X.; Sun, Y.; Tang, C.; Wang, Z.; Su, Y.; Li, Y. Dynamic parameters identification method for inductively coupled power transfer system. In Proceedings of the 2010 IEEE International Conference on Sustainable Energy Technologies (ICSET), Kandy, Sri Lanka, 6–9 December 2010.
23. Chow, J.P.-W.; Chung, H.-H.; Cheng, C.-S.; Wang, W. Use of Transmitter-Side Electrical Information to Estimate System Parameters of Wireless Inductive Links. *IEEE Trans. Power Electron.* **2017**, *32*, 7169–7186. [CrossRef]
24. Chow, J.P.W.; Chung, H.S.H.; Cheng, C.S. Use of Transmitter-Side Electrical Information to Estimate Mutual Inductance and Regulate Receiver-Side Power in Wireless Inductive Link. *IEEE Trans. Power Electron.* **2016**, *31*, 6079–6091. [CrossRef]
25. Xu, L.; Chen, Q.; Ren, X.; Wong, S.C.; Tse, C.K. Self-Oscillating Resonant Converter With Contactless Power Transfer and Integrated Current Sensing Transformer. *IEEE Trans. Power Electron.* **2017**, *32*, 4839–4851. [CrossRef]